Citation:
Ye, Y and Zhang, S-J and Zhou, K and Guo, Z-X (2021) Numerical study on behavior of eccentrically loaded concrete-filled bimetallic tubes. Structures, 36. pp. 935-950. ISSN 2352-0124 DOI: https://doi.org/10.1016/j.istruc.2021.12.053

Link to Leeds Beckett Repository record:
https://eprints.leedsbeckett.ac.uk/id/eprint/8342/

Document Version:
Article (Accepted Version)

Creative Commons: Attribution-Noncommercial-No Derivative Works 4.0

The aim of the Leeds Beckett Repository is to provide open access to our research, as required by funder policies and permitted by publishers and copyright law.

The Leeds Beckett repository holds a wide range of publications, each of which has been checked for copyright and the relevant embargo period has been applied by the Research Services team.

We operate on a standard take-down policy. If you are the author or publisher of an output and you would like it removed from the repository, please contact us and we will investigate on a case-by-case basis.

Each thesis in the repository has been cleared where necessary by the author for third party copyright. If you would like a thesis to be removed from the repository or believe there is an issue with copyright, please contact us on openaccess@leedsbeckett.ac.uk and we will investigate on a case-by-case basis.

Numerical study on behavior of eccentrically loaded concrete-filled bimetallic tubes

Yong Ye [a, b *], Shi-Jiang Zhang [a], Kan Zhou [c], and Zi-Xiong Guo [a, b]

[a] *College of Civil Engineering, Huaqiao University, Xiamen, 361021, P. R. China*

[b] *Key Laboratory for Structural Engineering and Disaster Prevention of Fujian Province, Xiamen, 361021, P. R. China*

[c] *School of Built Environment, Engineering and Computing, Leeds Beckett University, City Campus, Leeds, LS1 3HE, UK*

*(*Corresponding author, E-mail address: qzyeyong@hqu.edu.cn)*

Abstract: The concrete-filled bimetallic tubular (CFBT) member studied in this paper comprises a stainless steel/carbon steel bimetallic tube infilled with core concrete. It has the advantages of enhanced mechanical property, good corrosion resistance and cost effectiveness. A finite element analysis (FEA) model is established to investigate the performance of eccentrically compressed CFBT short columns with a circular cross-section. The model is verified against the experimental results presented in a companion paper. The comparisons show that the FEA model reproduces reasonably well the failure mode, load-deformation response, ultimate strength and strain development of the composite member. The validated model is then used to further investigate the performance of eccentrically loaded CFBT members, followed by a wide-range parametric analysis. Results indicate that the two layers of the bimetallic tube attain their ultimate strength before the concrete core. The material strength shows a major effect on the ultimate strength of CFBT members, whilst the coefficient of friction for the interface between different materials and the strain-hardening exponent of stainless steel have a minor influence. Finally, the applicability of various design codes is explored and the comparisons show that the load-carrying capacity predicted by AISC360-16 is conservative, whilst Eurocode 4 and DBJ/T13-51-2010 produce relatively accurate predictions.

Keywords: Concrete-filled bimetallic tube; Eccentric compression; Numerical model; Load-carrying capacity; Interaction curve

1. Introduction

Concrete-filled steel tubular (CFST) structural members are extensively used in practical engineering owing to their favorable mechanical and constructional performance [1]. In the applications of CFST structures, the normally adopted carbon steel tubes could be subjected to some harsh conditions, such as offshore and marine environments. Increasing requirements of inspection and maintenance for carbon steel tubes are needed when the CFST members are exposed to water or chemical substances, and this might disadvantage the traditional CFST structures on a whole-life-cycle basis.

Stainless steel is favorable for its excellent corrosion resistance, durability and ease of maintenance, and has potential to be widely used in structural engineering [2]. However, the cost of stainless steel is still much higher than the traditional carbon steel, and this significantly suppresses the widespread application of stainless steel at this stage. Aiming at promoting the more effective and economical use of stainless steel, the stainless steel/carbon steel bimetallic material is produced by combining a substrate carbon steel layer and a cladding stainless steel layer through various techniques and processes [3, 4]. So far, research on the properties of bimetallic material under various conditions is available [5-11].

With the aim of fully developing the advantages of bimetallic material when it is adopted in structural engineering, the concrete-filled bimetallic tubular (CFBT) member was proposed by Ye et al. [12]. The CFBT member consists of a bimetallic tube and the infilled concrete. The bimetallic tube is manufactured by cladding a carbon steel tube with a thin-walled stainless steel layer. By adopting this combination of different metals, the favorable corrosion resistance and cost-efficiency of bimetallic tubes could become more competitive than either pure carbon steel tubes or stainless steel tubes when considering the whole-life-cycle benefit.

To investigate the structural performance of CFBT members, Ye et al. [13, 14] and Zhang et al. [15]

performed a series of experimental studies on the behavior of CFBT short columns subjected to either axial or eccentric loading. The experimental results confirmed the effective confinement provided by the bimetallic tube to the concrete core and the corresponding composite actions between the two components. However, the influence of different parameters on the load-carrying capacity of CFBT members under eccentric compression, and the corresponding design method still need to be investigated.

Based on the above research background, this paper reports a numerical analysis on the structural behavior of eccentrically compressed CFBT short columns. The objectives of this research are threefold: firstly, to establish a nonlinear 3-D finite element analysis (FEA) model of circular CFBT short columns subjected to eccentric compression; secondly, to further analyze the structural performance of CFBT columns with different load eccentricity, including the failure mode, the full-range load-deformation response, and the load distribution and contact stress between the two contacted components; and thirdly, to evaluate the design models in existing codes for computing the ultimate load capacity of CFBT short columns.

2. Establishment of the FEA model

2.1 General information

2.1.1 Available test data of CFBT specimens under eccentric compression

The authors of this paper conducted an experimental investigation consisting of six hollow bimetallic tubes and six CFBT specimens subjected to eccentric compression [15]. The main test results are listed in Table 1, where f_{cu} is the cube compressive strength of concrete; e_n is the nominal eccentric distance; D is the outer diameter of tube section; $N_{u,e}$ is the experimental ultimate load capacity; and $N_{u,FEA}$ is the FEA-predicted ultimate strength. The tube length (L) of all the CFBT and hollow bimetallic tube specimens was 350 mm and the outer diameter (D) of the section was 114 mm. The

wall thickness of the outer tube-layer (stainless steel, t_{ss}) and inner tube-layer (carbon steel, t_{sc}) were 1.0 mm and 2.0 mm, respectively, resulting in a total thickness of the bimetallic tube (t_{total}) of 3.0 mm.

2.1.2 Type of elements and mesh size

The FEA model of the circular CFBT specimens under eccentric loading was established by adopting the FEA program ABAQUS (Version 6.14) [16]. The concrete core, end plates and stiffeners of the specimens were modelled using eight-node brick elements (C3D8R). The two layers of the bimetallic tube were modelled separately, and four-node 3D shell elements (S4R) were employed due to the thin-walled characteristic. To achieve a considerable balance between the computational accuracy and efficiency, convergence analysis was performed to determine the appropriate dimensions of the mesh for different components. Based on the convergence analysis, the mesh dimension for the infilled concrete and the two tube-layers was set as 15 mm in the current modelling. The schematic diagram of the meshed FEA model with the selected dimensions is depicted in Fig. 1.

2.1.3 Interfacial behavior

To replicate the interaction behavior between the steel tube and the concrete core, an interface model combining the "hard" contact model in the normal direction and the Coulomb friction model along the tangential direction was utilized. Based on the previous research [17], the coefficient of friction for the carbon steel-concrete interface was taken as 0.6.

In practice, various techniques and processes can be adopted to fabricate the bimetallic tubes [18], mainly including the mechanical combination and metallurgic combination of two different types of metals. The stainless steel (outer)-carbon steel (inner) bimetallic tube in this research was obtained by combining the two different tube-layers with the mechanically cladding method. The carbon steel tube was cladded with a stainless steel layer and no special surface treatment was taken in the previous experimental study [15], where no phenomenon of separation of the two tube-layers was observed

during testing. To be consistent, the two tube-layers were modelled individually but with a definition of the interfacial behavior herein. Since there was no additional bond at carbon steel-stainless steel interface, the interface model combining the Mohr-Coulomb friction (tangential direction) and the "hard" contact (normal direction) was also used to describe the interfacial behavior. The coefficient of friction for the carbon steel-stainless steel interface was set to be 0.8 [19]. As for those bimetallic tubes manufactured by metallurgic combination, the two tube-layers could be strongly combined with sufficient bond in the interface. In that case, the "tie" function in ABAQUS would be suitable for modelling the interface between the two tube-layers of a bimetallic tube.

The end-plates as well as the stiffeners were welded at both ends of the bimetallic tubes in the previous experiments [15]. As a result, a perfect bond was considered in the matched interface between the bimetallic tube, stiffeners, and end-plates, and the perfect bond was realized by adopting the "tie" method in ABAQUS. The above-mentioned interface model was also employed for the steel tube-concrete core interface, but the value of friction coefficient was taken as 0.6.

2.1.4 Loading and boundary conditions

The eccentric compression was applied to the loading line at the top surface of the upper end-plate, as shown in Fig. 1. Along the fixed line located at the bottom surface of the specimen, all degrees of freedom (DOFs) were restrained except for the rotation around *x* axis, while all DOFs except for the translation along *z* axis and the rotation around *x* axis were restrained along the loading line located at the top surface of the upper end-plate. The loading line and fixed line had the same eccentric distance (*e*) to the symmetric axis. The load was applied to the loading line along *z* axis with a displacement-controlled mode to achieve better convergence of computation.

2.1.5 Consideration of initial imperfection

During the fabrication process, initial imperfections, such as geometric error and residual stress

related to the steel tube, are often inevitable in CFST members [20]. Previous research indicated that, local geometric error and residual stress have a significant effect on the performance of hollow steel tubes [21], while a marginal influence on the performance of conventional CFST members [22, 23]. The gap between the steel tube and concrete core could delay the composite actions in CFST members under some extreme conditions [24], while careful concrete casting and vibration can effectively avoid this possible imperfection. Thus, the influence of the concrete imperfection was not considered, and only the imperfection in tubes was taken into account herein. To validate the proposed FEA model and replicate the results obtained from experiments, it is necessary to consider a proper pattern and assume an amplitude factor for the initial geometric imperfection along the entire tube. The imperfection was simulated through eigenvalue buckling analysis of the hollow bimetallic tube [25]. The results of eigenvalue buckling analysis were then linked to the FEA model by adopting the "IMPERFECTION" method in ABAQUS. The amplitude of geometric imperfection was set as $t_{total}/100$, which was adopted in the simulation of both hollow stainless steel sections [26] and concrete-filled stainless steel tubular specimens [27].

2.2 Material models

2.2.1 Carbon steel

For the carbon steel, an isotropic elastic-nonlinear plastic behavior with a von Mises yield surface and the associated plastic flow was used in the FEA modelling. A five-stage stress (σ) versus strain (ε) response reported by Han [28] was used to describe the uniaxial σ-ε curve of carbon steel, as depicted in Fig. 2(a), where f_p is the limit of proportionality, ε_p is the strain corresponding to f_p, f_y is the yield strength, ε_{y1} and ε_{y2} are the strains at the beginning and end of the yield plateau, f_u is the ultimate strength, and ε_u is the strain corresponding to f_u.

2.2.2 Stainless steel

Compared to the mild carbon steel with an obvious yielding stage, stainless steel exhibits a typical nonlinear response with a continuous strain-hardening feature. The Ramberg-Osgood model [29] was proposed to illustrate the σ-ε relationship of austenitic stainless steel, as follows:

$$\varepsilon = \frac{\sigma}{E_0} + 0.002\left(\frac{\sigma}{\sigma_{0.2}}\right)^n \tag{1}$$

where E_0 is the Young's modulus, n is the factor related to the strain-hardening response from $\sigma_{0.01}$ to $\sigma_{0.2}$, and $\sigma_{0.01}$ and $\sigma_{0.2}$ are the 0.01% and 0.2% proof stress, respectively.

Previous research [30] has indicated that the Ramberg-Osgood model in Eq. (1) provides an accurate prediction of the σ-ε relationship for a stress up to $\sigma_{0.2}$, while gives a prediction that remarkably deviates from the experimental results when the stress is greater than $\sigma_{0.2}$. Therefore, an improved model [30] was used for stainless steel when the stress exceeds $\sigma_{0.2}$. Consequently, the σ-ε response of stainless steel was described by a two-stage equation, as illustrated in Fig. 2(b) and expressed as follows:

$$\varepsilon = \frac{\sigma}{E_0} + 0.002\left(\frac{\sigma}{\sigma_{0.2}}\right)^n \qquad (\sigma \le \sigma_{0.2}) \tag{2-a}$$

$$\varepsilon = \frac{\sigma - \sigma_{0.2}}{E_{0.2}} + \varepsilon_{ss,u}\left(\frac{\sigma - \sigma_{0.2}}{\sigma_{ss,u} - \sigma_{0.2}}\right)^m + \varepsilon_{0.2} \qquad (\sigma > \sigma_{0.2}) \tag{2-b}$$

where $\varepsilon_{0.2}$ is the strain corresponding to $\sigma_{0.2}$, $\sigma_{ss,u}$ is the ultimate strength, $\varepsilon_{ss,u}$ is the ultimate strain corresponding to $\sigma_{ss,u}$, $E_{0.2}$ is the tangent modulus corresponding to $\sigma_{0.2}$, m is the factor related to the strain-hardening from $\sigma_{0.2}$ to $\sigma_{ss,u}$.

2.2.3 Concrete

The damage plastic model was adopted to simulate the concrete in the FEA modelling. Considering the concrete confined by the bimetallic tube was similar to that confined by the carbon steel tube in a conventional CFST member, the uniaxial stress (σ) versus strain (ε) relationship suggested by Han

[17] was adopted to express the compressive behavior of the core concrete [see Fig. 2(c)], which is expressed as:

$$y=\begin{cases}2x-x^2 & x\le 1\\ \dfrac{x}{\beta_0(x-1)^2+x} & x>1\end{cases} \tag{3}$$

where $y=\sigma/f_c'$, f_c' is the concrete cylinder strength; $x=\varepsilon/\varepsilon_0$, ε_0 is the strain corresponding to f_c', $\varepsilon_0=(1300+12.5f_c'+800\xi_{CFBT}^{0.2})\times10^{-6}$; ξ_{CFBT} is the confinement factor for CFBT members, $\xi_{CFBT}=(A_{sc}f_y+A_{ss}\sigma_{0.2})/(A_c f_{ck})$ [13], A_{sc}, A_{ss} and A_c are the cross-sectional areas of the carbon steel tube-layer, stainless steel tube-layer, and concrete core, respectively, f_{ck} is the characteristic concrete strength, $f_{ck}=0.67f_{cu}$, f_{cu} is the cube strength of concrete; β_0 is the factor related to the confinement factor and ultimate strength of concrete, $\beta_0=(1.18\times10^{-5})^{[0.25+(\xi_{CFBT}-0.5)^7]}(f_c')^{0.5}\ge0.12$.

For the tension behavior of concrete, a fracture energy-based approach was adopted to simulate the tensile softening performance of concrete, and the fracture energy of concrete (G_F) was defined as follows [31]:

$$G_F=73f_c^{0.18} \tag{4}$$

2.3 Verifications

2.3.1 Failure modes

The established FEA model for circular CFBT short columns under eccentric loading was validated by replicating the experimental results reported in a companion paper [15]. A comparison of failure models between the numerical and test results is depicted in Fig. 3. Good agreements were generally found between the FEA prediction and measured results for both the CFBT and hollow bimetallic tube (BT) specimens. For the BT specimens, an obvious inward local buckling occurred near the mid-height section [Fig. 3(a)], while overall bending was observed in the CFBT specimens [Fig. 3(b)]. The comparison of concrete cracking patterns between the prediction and experimental observation

for the CFBT specimens (CFBT-e0.26-1 and CFBT-e0.79-1) was shown in Fig. 3(c) and 3(d), where the vector stands for the magnitude and path of the maximum principal plastic strain ($\varepsilon_{pe,max}$). The concrete cracking could be predicted by $\varepsilon_{pe,max}$ in the FEA modelling and cracks appear perpendicularly with respect to the direction of $\varepsilon_{pe,max}$. A similar distribution of concrete crushing and crack patterns between the numerical simulation and test results is shown in Fig. 3(c) and 3(d), where the vector distribution indicates that the concrete core is crushed in the compressive side and flexural cracks appeared in the tensile side.

2.3.2 Ultimate strength

The comparisons of load (N) vs. axial deformation (Δ) relationships and moment (M) vs. end plate rotation (θ) curves are shown in Fig. 4 and Fig. 5, respectively. An acceptable accuracy between the FEA calculation and measured results was observed when considering the overall trend of the N-Δ and M-θ curves for both CFBT and BT specimens. Additionally, the accuracy of the FEA model for simulating the structural performance of CFST members under pure bending moments was validated using the available experimental results [32], as illustrated in Fig. 6, where ε_{max} is the maximum fiber strain, and the moment capacity is determined corresponding to an ε_{max} of 10,000 με.

The comparison of ultimate bearing capacity between the FEA calculations ($N_{u,FEA}$) and measured results ($N_{u,e}$) is depicted in Fig. 7, and the corresponding values are recorded in Table 1. The average value of $N_{u,FEA}/N_{u,e}$ is 1.037 with a standard deviation of 0.064, indicating the numerical calculation generally agrees well with the experimental results.

2.3.3 Load-strain response

The comparisons of load (N) vs. longitudinal steel strain (ε_s) curves between the FEA and tested results are presented in Fig. 8, where $\varepsilon_{cl,c}$ and $\varepsilon_{tl,c}$ are the longitudinal compressive and tensile strains of carbon steel tube-layer; $\varepsilon_{cl,s}$ and $\varepsilon_{tl,s}$ are the longitudinal compressive and tensile strains of stainless

steel tube-layer; and $\varepsilon_{cl,FEA}$ and $\varepsilon_{tl,FEA}$ are the FEA-predicted longitudinal compressive and tensile strains. It can be seen that, the development of the longitudinal compressive and tensile steel strains in the numerical model generally agree well with the experimental results. For the specimens with a load eccentric distance (e) equal to 4 mm, the strain at the tensile zone is negative during loading and transforms to positive at the ultimate strength for both the CFBT and BT short columns [Fig. 8(a) and 8(e)]. For the BT specimens at the ultimate load, the strain in the tensile side does not attain the yield strain except for the specimen with an e/D-value equal to 0.79 [Fig. 8(d)]. For the CFBT specimens with an e/D-value greater than 0.26, the longitudinal strain at both the compressive and tensile zones excess the yield strain [Fig. 8(f)-8(h)]. Therefore, it is reasonable to assume that for circular BT and CFBT short columns subjected to eccentric loading, the yield strength of the carbon steel and the stainless steel could be generally fully utilized.

Based on the above comparisons, the accuracy of the established FEA model is well validated. Hence, it is reasonable to employ the FEA model to further investigate the structural performance of CFBT columns under eccentric loading.

3. Analytical behavior

In this section, the numerical result is presented for extensive analysis of the performance of circular CFBT short columns, mainly including the load distribution and contact stress between different components, and the longitudinal stress of different components at the mid-height section.

3.1 Load distribution

The load (N) vs. axial deformation (Δ) responses of different components in the CFBT short columns with different load eccentricities (e/D) are depicted in Fig. 9, where N is the vertical load at the mid-height cross-section that obtained through the "free body diagram" method. As expected, the concrete core bears the majority of the external load applied to the composite member. The N-Δ curves could

be divided by four characteristic points (A to D) into four stages:

(1) Stage 1 (OA). The linearly elastic stage. Before reaching Point A, the loads carried by all the components increase almost linearly as the axial deformation (Δ) increases. The N-Δ response for the carbon steel tube-layer reaches its ultimate compressive load at Point A; while for the stainless steel tube-layer, the curve almost attains its ultimate compressive load. The initial yielding of the bimetallic tube on the compressive side has occurred at the same time.

(2) Stage 2 (AB). The N-Δ curve for the whole composite section attains its ultimate load capacity at Point B. The load carried by the concrete core increases with a decreasing rate over this stage. Meanwhile, the load carried by the bimetallic tube decreases fast. For the specimen with $e/D \geq 0.53$, a tensile load even appears [Fig. 9(c) and 9(d)]. This indicates that the main contribution of the bimetallic tube turns from directing bearing the external load to confining the core concrete.

(3) Stage 3 (BC). The load carried by the core concrete increases slightly and attains its ultimate value at Point C, whereas the loads carried by the carbon steel tube-layer and stainless steel tube-layer don't change much at this stage.

(4) Stage 4 (CD). Point D represents the termination of the loading process. The loads carried by different components tend to decrease slightly over this stage, showing ductile behavior of this composite member in the post-peak loading stage.

3.2 Contact stress between different components

The contact stresses between different components of the CFBT specimens are illustrated in Fig. 10, where $p_{c\text{-}s}$ is the contact stress in the interface between the carbon steel tube-layer and concrete core, and $p_{s\text{-}s}$ is the contact stress in the interface between the two tube-layers.

During the loading process, $p_{c\text{-}s}$ and $p_{s\text{-}s}$ in the compressive and tensile zones exhibit an increasing trend. Meanwhile, as the load eccentricity (e/D) increases, the values of $p_{c\text{-}s}$ and $p_{s\text{-}s}$ on the

compressive side tend to decrease. For the CFBT with an e/D-value less than 0.53, the magnitude of $p_{c\text{-}s}$ and $p_{s\text{-}s}$ on the tensile side decreases; while for the CFBT with an e/D value greater than 0.53, the opposite trend is observed. This is because as the e/D-value increases, the failure of eccentrically compressed CFBT members shifts from compression-controlled failure to tension-controlled failure. Besides, the value of $p_{c\text{-}s}$ is approximately 2 times greater than that of $p_{s\text{-}s}$. This is within expectation, because the closer to the interface between the carbon steel tube-layer and the concrete core, the greater the deformation/strain that the tube materials undergo. The results suggest that the inner carbon steel tube-layer is more crucial than the outer stainless steel tube-layer in terms of providing lateral confinement to the concrete core. This also confirms the effective confinement offered by the outer stainless steel tube-layer and the composite actions between different components in the eccentrically compressed CFBT members.

3.3 Concrete stress

The longitudinal stress (s33) distribution of the concrete core across the mid-height cross-section at the ultimate state are depicted in Fig. 11, where the dash-dotted line represents the neutral axis. It shows that the concrete stress increases gradually from the neutral axis to the edge of the concrete core. Within the test parameters herein (e/D=0-0.79), the neutral axis tends to shift from the edge to the middle as the e/D-value increases. Moreover, comparing the CFBT member with an e/D-value of 0.79 and that with an e/D-value of 0.26, it shows that s33 on the compressive side of the former is smaller than that of the latter. This suggests that as the e/D-value increases, the confinement supplied by the outer bimetallic tube to the concrete core at the compressive zone tends to decrease and the corresponding load-carrying capacity of the concrete core weakens. Moreover, s33 in the compressive zone of concrete core exceeds the cylinder compressive strength of the unconfined concrete (f_c'=44.4 MPa), which demonstrates that the core concrete is efficiently confined by the outer bimetallic tube

and the compressive strength is enhanced.

3.4 Steel stress

Considering the compatible deformation of the two layers of the bimetallic tube, the strain development of the two tube-layers is considered the same. Hence, only the longitudinal stress of the stainless steel tube-layer is studied in this section, as depicted in Fig. 12. For the CFBT member with a load eccentric distance (e) equal to 4 mm (CFBT-1), the mid-height cross-section is entirely subjected to compression when the magnitude of external load is less than $0.8N_u$, as shown in Fig. 12 (a). For the CFBT member with an e/D-value less than 0.53, the stresses at the compressive side develop more rapidly than those at the tensile side, while a different trend occurs in the CFBT member with an e/D-value greater than 0.53. This phenomenon shows that the failure of eccentrically compressed CFBT members changes from the compression-controlled mode to the tension-controlled mode with the increase of e/D. Additionally, the distributions of longitudinal stress in the stainless steel tube-layer have confirmed the fact that the "plane section assumption" is suitable for the CFBT members subjected to eccentric loading.

3.5 Parametric analysis

To complement the experimental investigation and extend the range of parameters, this section conducts a wide-range parametric analysis. In terms of the material properties and geometric sizes of specimens, the parameters that were kept unchanged included: D=114 mm, L=350 mm, t_{total}=3.0 mm, the elastic modulus of carbon steel (E_{sc}) and stainless steel (E_{ss}) 202 GPa and 190 GPa, respectively, the Poisson's ratio of carbon steel (υ_{sc}) and stainless steel (υ_{ss}) both 0.3. The variable parameters were: e/D ranging from 0 to 1.0 (including concentric compression and pure bending), the wall thickness ratio between the stainless steel tube-layer and the bimetallic tube (t_{ss}/t_{total}) ranging from 0 to 1.0, f_y ranging from 235 MPa to 590 MPa, $\sigma_{0.2}$ ranging from 200 MPa to 600 MPa, f_{cu} ranging from 30 MPa

to 90 MPa, n ranging from 3 to 11, the coefficient of friction for the interface between the carbon steel and stainless steel tube-layers (μ) ranging from 0.2 to 0.8, the confinement coefficient (ξ) [13] ranging from 0.487 to 1.676.

3.5.1 Influence of load eccentricity

The ultimate strength of CFBT members with different values of e/D is shown in Fig. 13(a). It shows that the ultimate load-carrying capacity of CFBT members is reduced with a gradually decreasing rate as the e/D-value increases. Take the basic model series t2t1 as examples to evaluate the effect of e/D on the N-Δ relationship of CFBT members, as shown in Fig. 13(b). The corresponding basic geometric parameters are: t_{sc}=2.0 mm and t_{ss}=1.0 mm. The material parameters are: f_{cu}=50 MPa, f_y=235 MPa, $\sigma_{0.2}$=300 MPa, n=5. Fig. 13(b) shows that the ultimate load-carrying capacity of CFBT members with load eccentricities of 1/8, 1/4, 1/2, 3/4, and 1.0 is reduced by 29.0%, 46.4%, 67.1%, 77.8%, and 83.9% when compared to the concentrically compressed CFBT short columns, respectively.

3.5.2 Influence of stainless steel grade

The effect of $\sigma_{0.2}$ on the N-Δ relations of eccentrically compressed CFBT short columns is illustrated in Fig. 14, where e/D=0.5 is adopted in the basic model t2t1-0.5, and the variable parameter $\sigma_{0.2}$ ranges from 200 MPa to 600 MPa. The results show that the shape of the N-Δ curves tend to have a higher plateau with the increase of $\sigma_{0.2}$. For the basic model t2t1-0.5 with a $\sigma_{0.2}$-value less than 400 MPa, N decreases slightly after reaching the peak with increasing Δ, whilst for the model with a $\sigma_{0.2}$-value greater than 400 MPa, N tends to remain constant or even increase after reaching the plateau. The ultimate and residual strengths of CFBT members almost improve linearly with the increase of $\sigma_{0.2}$, while the initial stiffness is affected by $\sigma_{0.2}$ to a little extent. Compared to the basic model t2t1-0.5, the ultimate strength of the model with a $\sigma_{0.2}$-value of 200 MPa is reduced by 11.6%, while the

ultimate strength of models with a $\sigma_{0.2}$-value of 400 MPa, 500 MPa, and 600 MPa are increased by 8.4%, 20.1%, and 26.9%, respectively.

Furthermore, compared to the basic model t2t1 with e/D=0.5, a variety of strain-hardening exponents of stainless steel, n, ranging from 3 to 11 were analyzed, as illustrated in Fig. 15. It shows that n has limited effect on the N-Δ curve of CFBT members, and a variation of 1.1% in the ultimate strength is obtained.

3.5.3 Influence of carbon steel strength

The influence of f_y on the N-Δ relationships of eccentrically compressed CFBT short members is shown in Fig. 16. It indicates that f_y has a similar effect with $\sigma_{0.2}$ on the N-Δ response. The ultimate load-carrying capacity of CFBT members increases significantly with the increase of f_y, while the initial stiffness almost keeps unchanged. Compared to the basic model t2t1-0.5, the ultimate load-carrying capacity of CFBT members with f_y of 335 MPa, 460 MPa, and 590 MPa are increased by 16.6%, 36.6%, and 55.1% when compared to the member with f_y=235 MPa, respectively.

3.5.4 Influence of concrete strength

The influence of f_{cu} on the N-Δ relationships of CFBT short columns under eccentric compression is shown in Fig. 17. It shows that as f_{cu} increases, the ultimate load capacity of CFBT members increases accordingly, while for the post-peak branch of the N-Δ curve, it tends to experience a steep decrease. The load generally levels off after reaching the peak value and retains a similar residual strength. Compared to the basic model t2t1-0.5, the ultimate strength of CFBT column with f_{cu}=30 MPa and 40 MPa are reduced by 11.7% and 4.9%, while the ultimate strength of CFBT column with f_{cu}=60 MPa, 70 MPa, 80 MPa, and 90 MPa is increased by 4.5%, 9.3%, 16.7%, and 22.5%, respectively.

3.5.5 Influence of wall thickness ratio

To achieve a good balance between cost efficiency in construction and corrosion resistance of CFBT

columns, the optimum amount of stainless steel used in the bimetallic tubes should be determined. Fig. 18 shows the effect of wall thickness ratio between the stainless steel tube-layer and the bimetallic tube (t_{ss}/t_{total}) on the N-Δ relationships of CFBT members. It shows that the shape of the N-Δ curves tend to have a higher plateau with the increase of t_{ss}/t_{total}. For the basic model t2t1-0.5 with a t_{ss}/t_{total}-value less than 0.5, N tends to decrease marginally with increasing Δ after reaching the ultimate strength, while N remains constant or even increases for the model with a t_{ss}/t_{total} value greater than 0.5. The ultimate strength and residual strength increase linearly when the t_{ss}/t_{total}-value increases from 0 to 1.0 with $\sigma_{0.2}/f_y$=1.28. However, an ultimate strength variation for some grades of stainless steel and carbon steel remains within 5.0%, demonstrating a slight influence of t_{ss}/t_{total} on the ultimate load-carrying capacity of eccentrically compressed CFBT members.

3.5.6 Influence of friction coefficient

Various values of friction coefficient (μ) have been assessed for the interface between the carbon steel tube-layer and the stainless steel tube-layer [19, 33]. The effect of μ on the N-Δ relationships of CFBT members under eccentric compression is shown in Fig. 19. It shows that μ has a minor effect on the N-Δ relationships, and a variation of 1.1% in the ultimate strength is obtained.

3.5.7 N_u-M_u interaction

The influences of different parameters on the N_u-M_u interaction are shown in Fig. 20, where N_u is the calculated ultimate load capacity of CFBT members under concentric compression and M_u is the predicted resistance of CFBT members subjected to pure bending. The M_u-value is defined as the bending moment corresponding to a ε_{max}-value of 10,000 με. Fig. 20 shows that the parameters, $\sigma_{0.2}$, f_y and f_{cu}, have a major influence on the ultimate bearing capacity of circular CFBT members, whilst the effect of n and μ are limited. Besides, the parameter t_{ss}/t_{total} can also exert a remarkable influence on the load-carrying capacity of CFBT members [Fig. 20(e)]. This is primarily because the carbon

steel and stainless steel can have different strength grades, and changing the t_{ss}/t_{total}-value is some kind similar to altering the overall strength of the bimetallic tube. Thus, the effect of t_{ss}/t_{total} on the load-carrying capacity of CFBT members is similar to that of $\sigma_{0.2}$, which is confirmed by comparing Fig. 20(e) with Fig. 20(a).

4. Calculation method of load-carrying capacity

Currently, there is no specific design model for predicting the axial load (N)-moment (M) interaction of CFBT members. The study herein has indicated that the structural performance of CFBT columns under eccentric compression is similar to that of traditional CFST members. Hence, the calculation methods for circular CFST members under eccentric loading in currently available codes such as AISC360-16 [34], Eurocode 4 [35], and DBJ/T13-51-2010 [36] were utilized to calculate the N-M interactions of circular CFBT columns. The equations in the above codes were modified by replacing the steel tubes with bimetallic tubes to account for the CFBT cross-section.

4.1 AISC360-16

According to AISC360-16 [34], the resistance of compact circular CFST cross-sections to combined axial force and bending moment can be predicted as follows:

when $P_r / P_c \geq 0.2$,

$$\frac{P_r}{P_c} + \frac{8}{9} \times \frac{M_r}{M_c} \leq 1.0 \tag{5}$$

when $P_r / P_c \leq 0.2$,

$$\frac{P_r}{2P_c} + \frac{M_r}{M_c} \leq 1.0 \tag{6}$$

where P_r and M_r are the required axial strength and flexural strength, respectively, adopting load and resistance factor design (LRFD) or allowable strength design (ASD) load combinations; P_c and M_c are the provided axial and flexural strength, given by $F_{cr}A_g$ and F_yZ, respectively; F_{cr} is the critical

stress; F_y is the specified minimum yield stress; A_g is the gross cross-sectional area of section; Z is the plastic section modulus about the axis of bending.

4.2 Eurocode 4

Based on Eurocode 4 [35], the resistance of circular CFST columns under combined compression and uniaxial bending is expressed by:

$$\frac{M}{M_{\mathrm{pl,N,Rd}}}=\frac{M}{\mu_{\mathrm{d}}M_{\mathrm{pl,Rd}}}\le\alpha_{\mathrm{M}} \tag{7}$$

where M is the greatest value of the end moments and the maximum bending moment within the column length; $M_{\mathrm{pl,N,Rd}}$ is the plastic bending resistance taking into account the normal force, given by $\mu_{\mathrm{d}}M_{\mathrm{pl,Rd}}$; $M_{\mathrm{pl,Rd}}$ is the plastic bending resistance and α_{M} is the coefficient considering the effect of different steel grades.

4.3 DBJ/T13-51-2010

Based on DBJ/T13-51-2010 [36], the N/N_{u}-M/M_{u} interactions of CFST columns under combined compression and uniaxial bending are presented as follows:

when $N/N_{\mathrm{u}}\ge 2\eta_0$,

$$\frac{N}{N_{\mathrm{u}}}+a\beta_{\mathrm{m}}\left(\frac{M}{M_{\mathrm{u}}}\right)\le 1 \tag{8}$$

when $N/N_{\mathrm{u}}\le 2\eta_0$,

$$-b\left(\frac{N}{N_{\mathrm{u}}}\right)^2-c\left(\frac{\mathrm{N}}{N_{\mathrm{u}}}\right)+\beta_{\mathrm{m}}\left(\frac{M}{M_{\mathrm{u}}}\right)\le 1 \tag{9}$$

where N is the required axial load; N_{u} is the axial strength, $N_{\mathrm{u}}=(1.14+1.02\xi)f_{\mathrm{ck}}$; M_{u} is the ultimate pure bending strength, $M_{\mathrm{u}}=\gamma_{\mathrm{m}}W_{\mathrm{scm}}f_{\mathrm{sc}}$; a, b, c, ζ_0 and η_0 are the coefficients correlated with the confinement factor, $a=1-2\eta_0$, $b=(1-\zeta_0)/\eta_0^2$, $c=2(\zeta_0-1)/\eta_0$, $\zeta_0=0.18\xi^{-1.15}+1$, $\eta_0=\begin{cases}0.5\text{-}0.245\xi & \xi\le 0.4\\ 0.1+0.14\xi^{\text{-}0.84} & \xi>0.4\end{cases}$; and β_{m} is the equivalent moment coefficient.

4.4 Verification of the available design codes

The comparison between the test results [15] and the calculated results using the above three codes is presented in Table 2, where $N_{u,AISC}$, $N_{u,EC4}$, and $N_{u,DBJ}$ denote the values calculated by adopting AISC360-16, Eurocode 4, and DBJ/T13-51-2010, respectively, and $N_{u,e}$ stands for the experimental results. As shown in Table 2, the predictions given by AISC360-16 are generally conservative, the mean values of $N_{u,AISC}/N_{u,e}$ and $M_{u,AISC}/M_{u,e}$ are 0.517 with a coefficient of variation (COV) of 0.243 and 0.617 with a COV of 0.054, respectively. By comparison, Eurocode 4 and DBJ/T13-51-2010 predict the ultimate strength of CFBT members with an improved accuracy. For the former, the mean values of $N_{u,EC4}/N_{u,e}$ and $M_{u,EC4}/M_{u,e}$ are 1.072 with a COV of 0.115 and 0.915 with a COV of 0.019, respectively. For the latter, the mean values of $N_{u,DBJ}/N_{u,e}$ and $M_{u,DBJ}/M_{u,e}$ are 0.953 with a COV of 0.091 and 0.876 with a COV of 0.015, respectively.

The calculated results using the above codes and the numerical results obtained from the FEA models are compared in Fig. 21. Two cases are presented herein: Fig. 21(a) is for the case in which the load eccentricity (e/D) equals to 0.26 and Fig. 21(b) is for the case where e/D=1.0. The range of the confinement factor (ξ) considered is from 0.487 to 1.676. Fig.21(a) shows that Eurocode 4 and DBJ/T13-51-2010 provide an increasingly conservative result as the ξ-value increases, which is similar to that for the CFBT members under concentric compression [13]. Additionally, AISC360-16 provides a relative stable but more conservative prediction compared with the former two codes.

By contrast, the prediction accuracy of these codes seems to exhibit different patterns when the e/D-value is 1.0, as illustrated in Fig. 21(b). Generally, the predictions provided by Eurocode 4 and AISC360-16 tend to be more accurate as the ξ-value increases within the range of parameters. For DBJ/T13-51-2010, however, the prediction exhibits a very stable trend as the ξ-value varies. This is possibly because the codes do not consider explicitly the effect of ξ on the structural performance of

CFBT columns under eccentric loading. As a result, to improve the accuracy of the design methods, there could still be some room for future study on the influence of confinement on the ultimate strength of CFBT columns under eccentric loading.

5. Conclusions

The performance of circular CFBT members under eccentric compression is investigated by using FEA modelling. Based on the analytical results reported in this paper, the main conclusions could be drawn as follows:

(1) A validated FEA model is established to simulate the performance of circular CFBT members under eccentric compression. The predicted failure modes, load-axial deformation curves, moment-end plate rotation curves, ultimate load capacity and strain development of steel agree well with the measured results. The average ratio of predicted strengths to measured ones is 1.037, with a standard deviation of 0.064.

(2) The load distribution versus deformation results suggest that the carbon steel tube-layer and the stainless steel tube-layer attain their ultimate strength almost simultaneously before the concrete core. The composite cross-section attains the overall ultimate strength at some time in between.

(3) The parametric analysis suggests that load eccentricity and material strengths exhibit the major effect on the ultimate strength of CFBT members under eccentric loading. The strain-hardening exponent of stainless steel and the coefficient of friction for the interface between two tube-layers have a minor effect. The influence of the wall thickness ratio between the stainless steel tube-layer and the bimetallic tube can be activated by adopting different strength combinations of stainless steel and carbon steel.

(4) The comparison among the calculated results and FEA predictions indicate that the ultimate load capacity predicted by AISC360-16 is highly conservative, whilst Eurocode 4 and DBJ/T13-51-2010

produce relatively accurate predictions for the strength of CFBT members under eccentric compression.

Acknowledgements

This research is supported by the National Natural Science Foundation of China (Grant No. 51808234) and the Natural Science Foundation of Fujian Province, China (Grant No. 2021J01286). The support is highly appreciated.

References

[1] Han LH, Li W, Bjorhovde R. Developments and advanced applications of concrete-filled steel tubular (CFST) structures: members. J Constr Steel Res 2014; 100: 211-28.

[2] Han LH, Xu CY, Tao Z. Performance of concrete filled stainless steel tubular (CFSST) columns and joints: summary of recent research. J Constr Steel Res 2019; 152: 117-31.

[3] Guo X, Tao J, Wang W, Li H, Wang C. Effects of the inner mould material on the aluminium-316L stainless steel explosive clad pipe. Mater Design 2013; 49: 116-22.

[4] Li W, Wen Q, Yang X, Wang Y, Gao D, Wang W. Interface microstructure evolution and mechanical properties of Al/Cu bimetallic tubes fabricated by a novel friction-based welding technology. Mater Design 2017; 134: 383-93.

[5] Dhib Z, Guermazi N, Gasperini M, Haddar N. Cladding of low-carbon steel to austenitic stainless steel by hot-roll bonding: microstructure and mechanical properties before and after welding. Mat Sci Eng A 2016; 656: 130-41.

[6] Liu BX, Yin FX, Dai XL, He JN, Fang W, Chen CX, Dong YC. The tensile behaviours and fracture characteristics of stainless steel clad plates with diff erent interfacial status. Mat Sci Eng A 2017; 679: 172-82.

[7] Liu XP, Bai RS, Uy B, Ban HY. Material properties and stress-strain curves for titanium-clad bimetallic steels. J Constr Steel Res 2019; 162: 105756.

[8] Ban HY, Bai RS, Yang L, Bai Y. Mechanical properties of stainless-clad bimetallic steel at elevated temperatures. J Constr Steel Res 2019; 162: 105704.

[9] Ban HY, Bai RS, Chung KF, Bai Y. Post-fire material properties of stainless-clad bimetallic steel. Fire Safety J 2020; 112: 102964.

[10] Ban HY, Zhu JC, Shi G, Zhang Y. Tests and modelling on cyclic behaviour of stainless-clad bimetallic steel. J Constr Steel Res 2020; 166: 105944.

[11] Ban HY, Zhu JC, Shi G. Cyclic loading tests on welded connections of stainless-clad bimetallic steel and modelling. J Constr Steel Res 2020; 171: 106140.

[12] Ye Y, Han LH, Sheehan T. Finite element analysis on axial compressive behavior of circular

concrete filled bimetal tubular short columns. Proceedings of 11th International Conference on Advances in Steel and Concrete Composite Structures, Beijing, China, December 2015.

[13] Ye Y, Han LH, Sheehan T, Guo ZX. Concrete-filled bimetallic tubes under axial compression: experimental investigation. Thin Wall Struct 2016; 108: 321-32.

[14] Ye Y, Zhang SJ, Han LH, Liu Y. Square concrete-filled stainless steel/carbon steel bimetallic tubular stub columns under axial compression. J Constr Steel Res 2018; 146: 49-62.

[15] Zhang SJ, Guo ZX, Ma DY, Ye Y. Performance of concrete-filled bimetallic tube (CFBT) short columns subjected to eccentric compression: experimental investigation. J Constr Steel Res 2021; 181: 106626.

[16] ABAQUS. ABAQUS Standard User's Manual, Version 6.14. Dassault Systèmes Corporation, Providence, RI, USA, 2014.

[17] Han LH, Yao GH, Tao Z. Performance of concrete-filled thin-walled steel tubes under pure torsion. Thin Wall Struct 2007; 45(1): 24-36.

[18] Fan ZS, Yu HP, Li CF. Plastic deformation behaviour of bi-metal tubes during magnetic pulse cladding: FE analysis and experiments. J Mater Process Tech 2016; 229: 230-43.

[19] Ye Y, Han LH, Guo ZX. Concrete-filled bimetallic tubes (CFBT) under axial compression: analytical behavior. Thin Wall Struct 2017; 119: 839-50.

[20] Liao FY, Han LH, He SH. Behaviour of CFST short column and beam with initial concrete imperfection: Experiments. J Constr Steel Res 2011; 67(12): 1922-35.

[21] Zhao O, Gardner L, Young B. Structural performance of stainless steel circular hollow sections under combined axial load and bending-Part 1: experiments and numerical modelling. Thin Wall Struct 2016; 101: 231-39.

[22] Sharif AM, Al-Mekhlafi GM, Al-Osta MA. Structural performance of CFRP-strengthened concrete-filled stainless steel tubular short columns. Eng Struct 2019; 183: 94-109.

[23] Sharif AM, Al-Mekhlafi GM, Al-Osta MA. Behaviour of circular stainless steel stub columns internally strengthened by longitudinal carbon steel bars. Eng Struct 2019; 199: 109617.

[24] Han LH, Ye Y, Liao FY. Effects of core concrete initial imperfection on performance of eccentrically loaded CFST columns. J Struct Eng-ASCE 2016; 142(12): 04016132.

[25] Lai ZC, Varma AH. Noncompact and slender circular CFT members: Experimental database, analysis, and design. J Constr Steel Res 2015; 106: 220-33.

[26] Zhao O, Gardner L, Young B. Structural performance of stainless steel circular hollow sections under combined axial load and bending-Part 2: Parametric studies and design. Thin Wall Struct 2016; 101: 240-48.

[27] Al-Mekhlafi GM, Al-Osta MA, Sharif AM. Behaviour of eccentrically loaded concrete-filled stainless steel tubular stub columns confined by CFRP composites. Eng Struct 2020; 205: 110113.

[28] Han LH. Concrete filled steel tubular structures: theory and practice (3rd edition). China Science Press, Beijing, China, 2016. (in Chinese).

[29] Ramberg W, Osgood WR. Description of stress-strain curves by three parameters. NACA Technical Note no. 902, USA, 1943.

[30] Rasmussen KJR. Full-range stress-strain curves for stainless steel alloys. J Constr Steel Res 2003; 59(1): 47-61.

[31] Fédération Internationale du Béton (fib). Model Code 2010-Final draft, vol. 1, fédération internationale du béton. Lausanne, Switzerland, 2012.

[32] Han LH. Flexural behaviour of concrete-filled steel tubes. J Constr Steel Res 2004; 60(2): 313-37.

[33] Patel VI, Hassanein MF, Thai HT, Abadi HA, Paton-Cole V. Behaviour of axially loaded circular concrete-filled bimetallic stainless-carbon steel tubular short columns. Eng Struct 2017; 147: 583-97.

[34] ANSI/AISC 360-16. Specification for Structural Steel Buildings. AISC Committee on Specifications, Chicago, USA, 2016.

[35] Eurocode 4. Design of composite steel and concrete structures, Part 1-1: general rules and rules for building. European Committee for Standardization, Brussels, Belgium, 2004.

[36] DBJ/T13-51-2010. Technical specifications for concrete-filled steel tubular structures (revised version). Housing and Urban-Rural Development Department of Fujian Province, Fuzhou, China, 2010. (in Chinese).

Figures

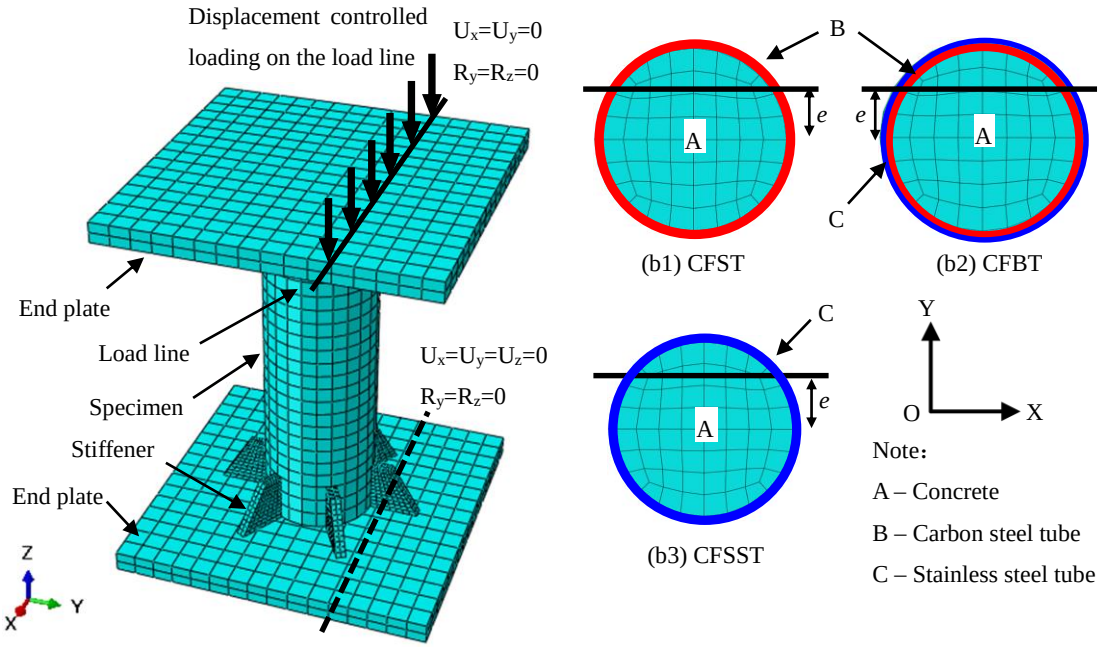

Fig. 1. Finite element model of different composite members.

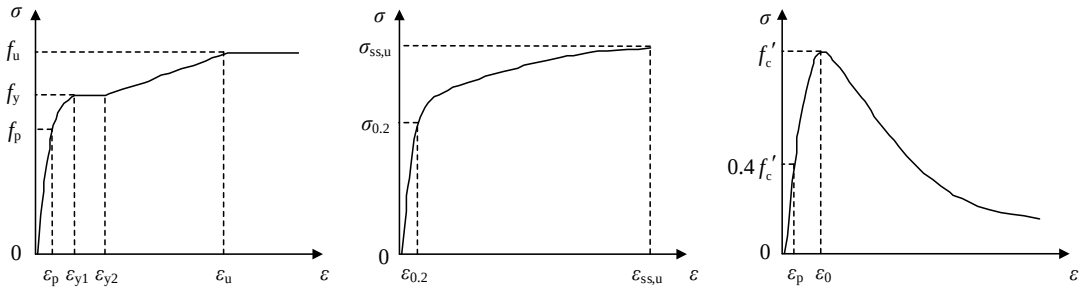

(a) (b) (c)

Fig. 2. Stress-strain relationships for different materials: (a) carbon steel; (b) stainless steel; (c) concrete.

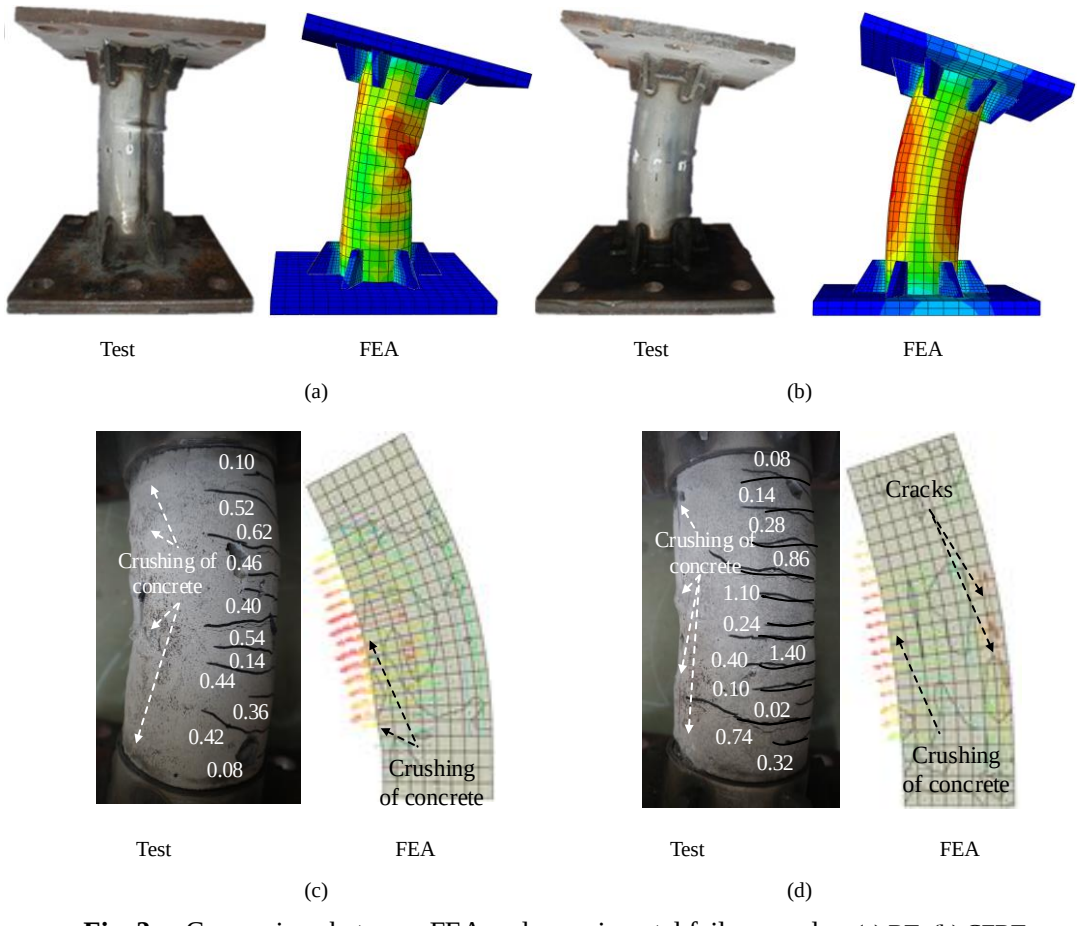

Fig. 3. Comparison between FEA and experimental failure modes: (a) BT; (b) CFBT; (c) CFBT-e0.26-1; (d) CFBT-e0.79-1.

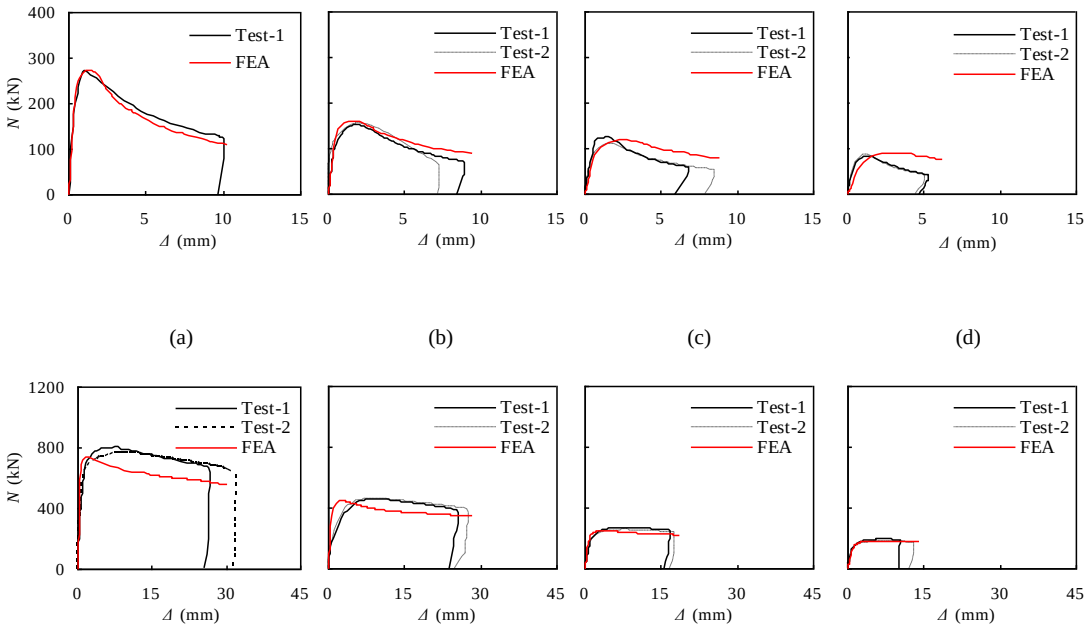

Fig. 4. Comparison between FEA and experimental *N*-*Δ* relationships: (a) BT-1; (b) BT-e0.26-1/2; (c) BT-e0.53-1/2; (d) BT-e0.79-1/2; (e) CFBT-1/2; (f) CFBT-e0.26-1/2; (g) CFBT-e0.53-1/2; (h) CFBT-e0.79-1/2.

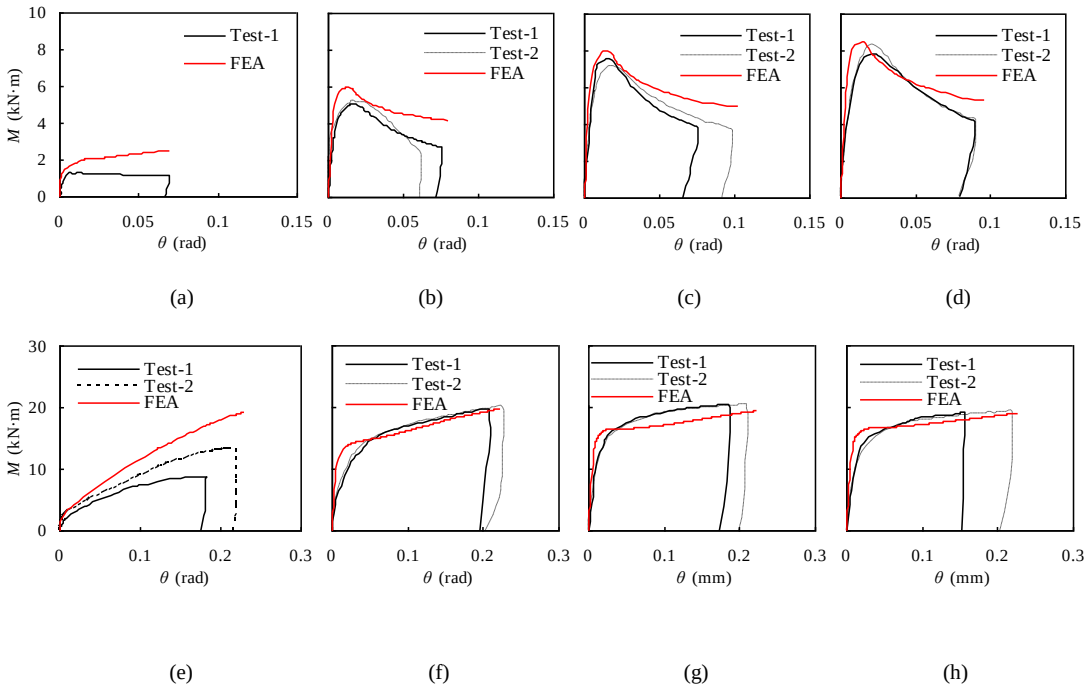

Fig. 5. Comparison between FEA and experimental *M*-θ relationships: (a) BT-1; (b) BT-e0.26-1/2; (c) BT-e0.53-1/2; (d) BT-e0.79-1/2; (e) CFBT-1/2; (f) CFBT-e0.26-1/2; (g) CFBT-e0.53-1/2; (h) CFBT-e0.79-1/2.

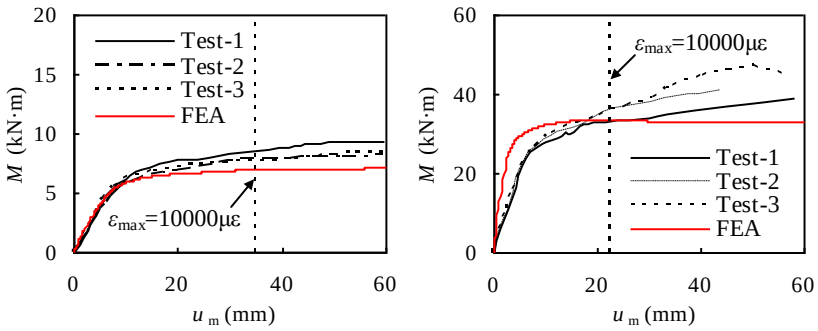

Fig. 6. Comparison between FEA and experimental M-u_m relationships: (a) CB1-1/2/3; (b) CB2-1/2/3.

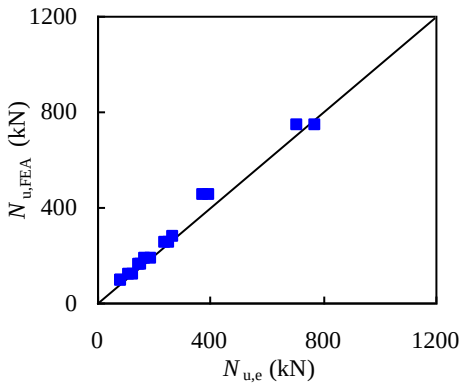

Fig. 7. Comparison between FEA ($N_{u,FEA}$) and experimental results ($N_{u,e}$).

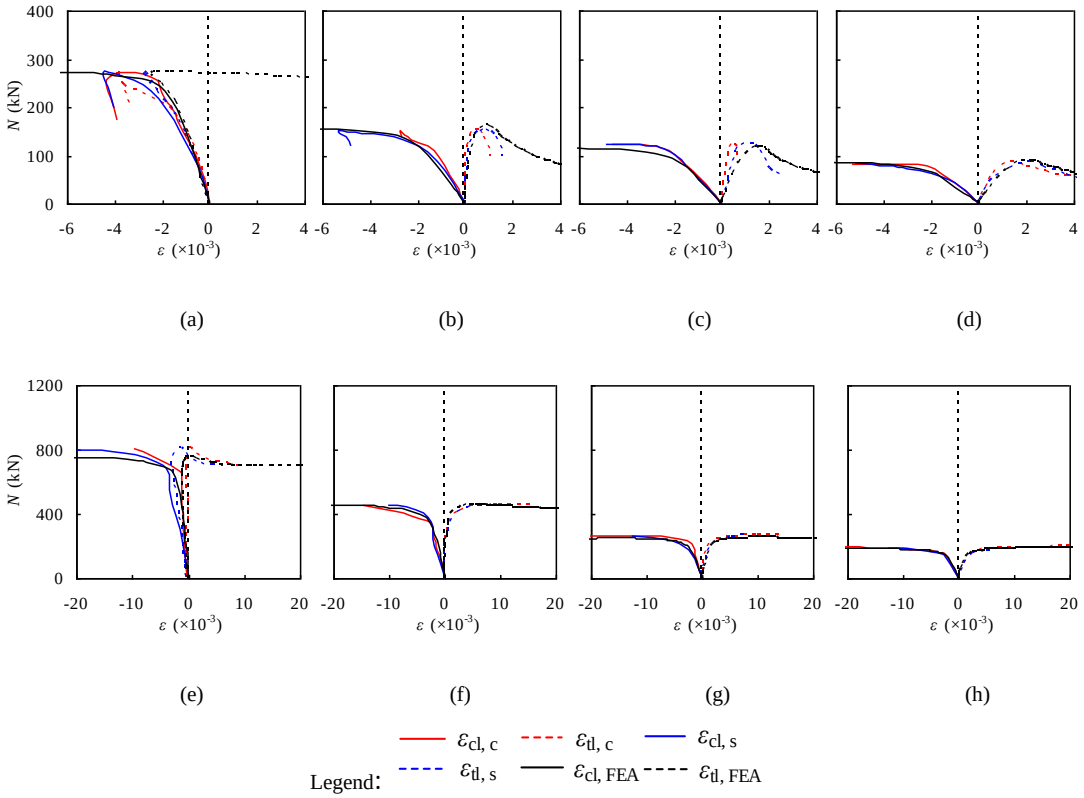

Fig. 8. Comparison between predicted and experimental N-ε_l curves: (a) BT-1; (b) BT-e0.26-1; (c) BT-e0.53-1; (d) BT-e0.79-2; (e) CFBT-2; (f) CFBT-e0.26-2; (g) CFBT-e0.53-1; (h) CFBT-e0.79-1.

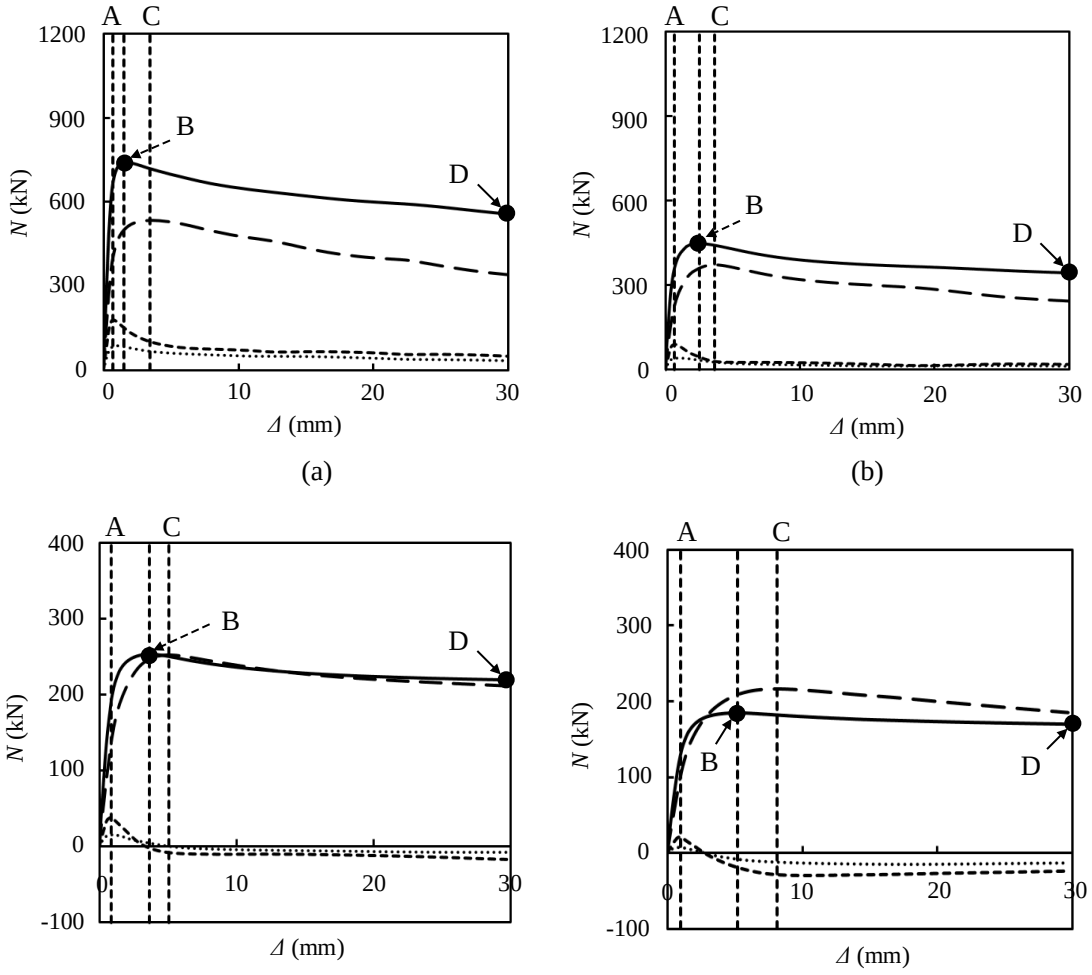

Fig. 9. Force distributions between different components: (a) CFBT-1; (b) CFBT-e0.26-1; (c) CFBT-e0.53-1; (d) CFBT-e0.79-1.

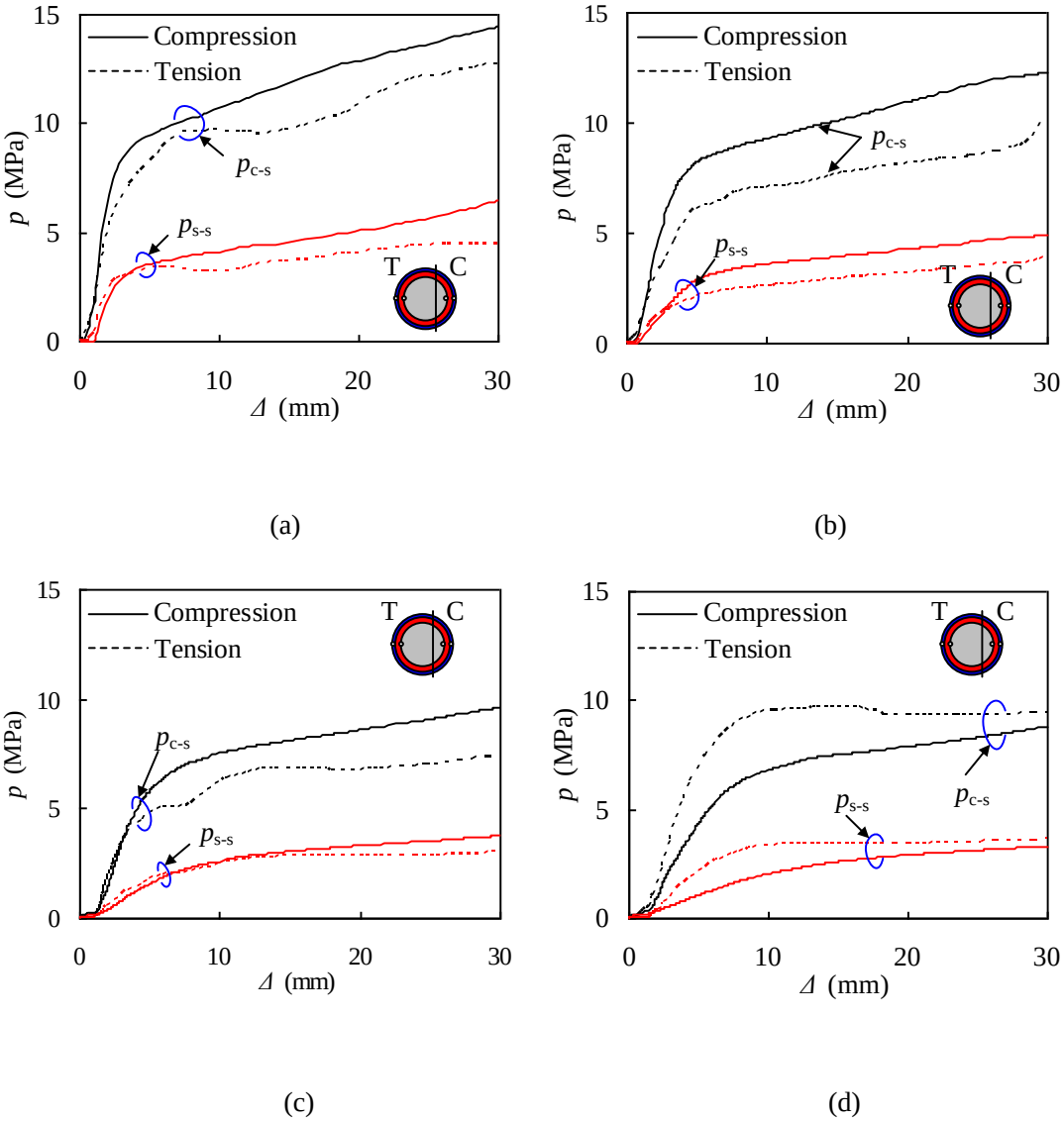

Fig. 10. Contact stress (p) versus axial deformation (Δ) curves: (a) CFBT-1; (b) CFBT-e0.26-1; (c) CFBT-e0.53-1; (d) CFBT-e0.79-1.

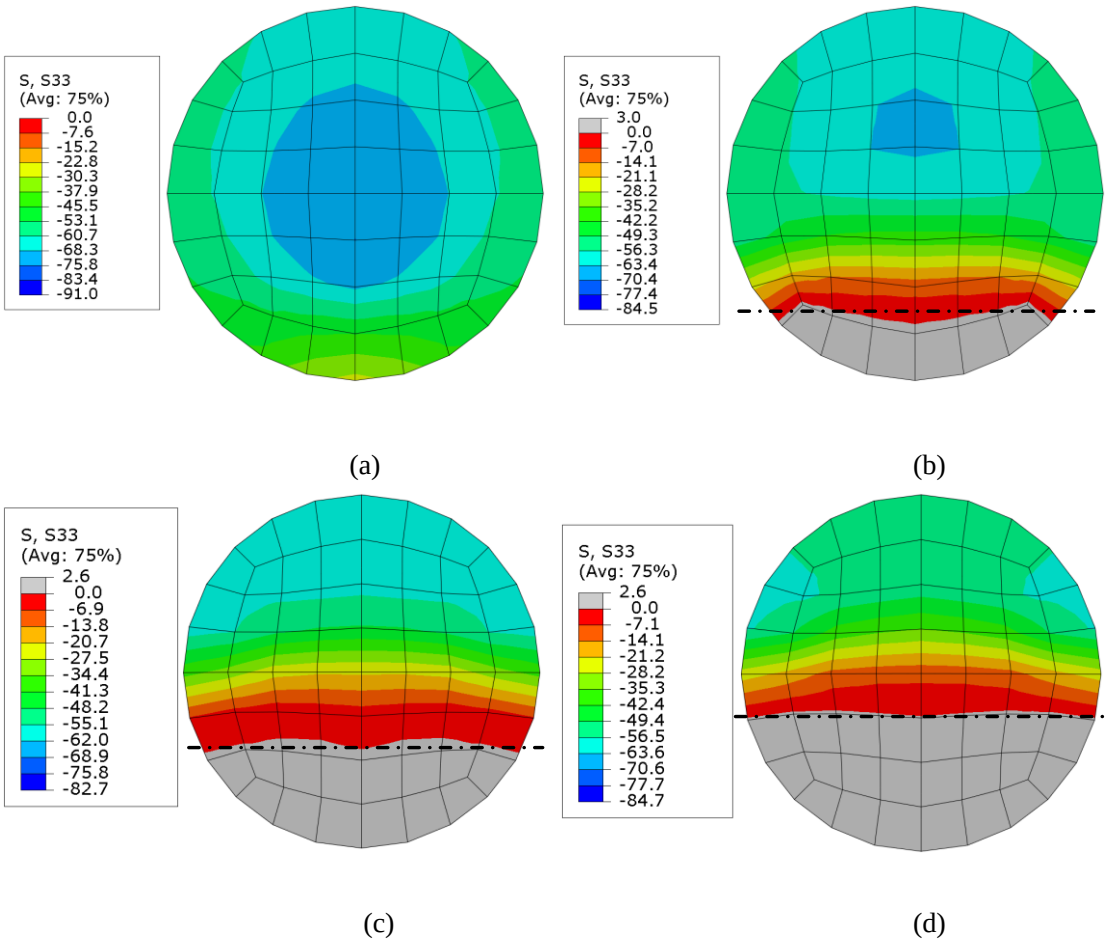

Fig. 11. Distribution of the longitudinal stress of concrete core at the ultimate state: (a) CFBT-1; (b) CFBT-e0.26-1; (c) CFBT-e0.53-1; (d) CFBT-e0.79-1.

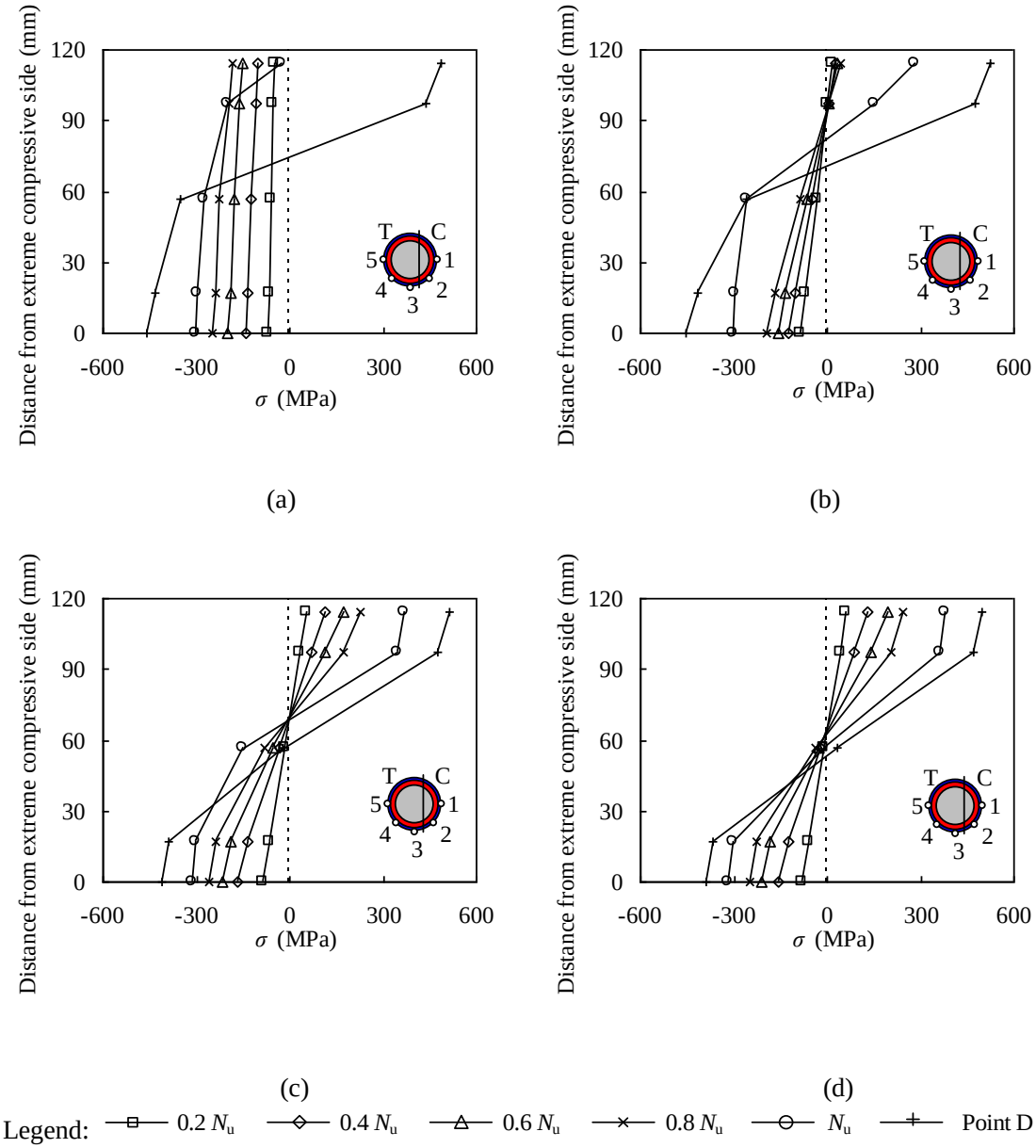

Fig. 12. Longitudinal stress of steel at mid-height: (a) CFBT-1; (b) CFBT-e0.26-1; (c) CFBT-e0.53-1; (d) CFBT-e0.79-1.

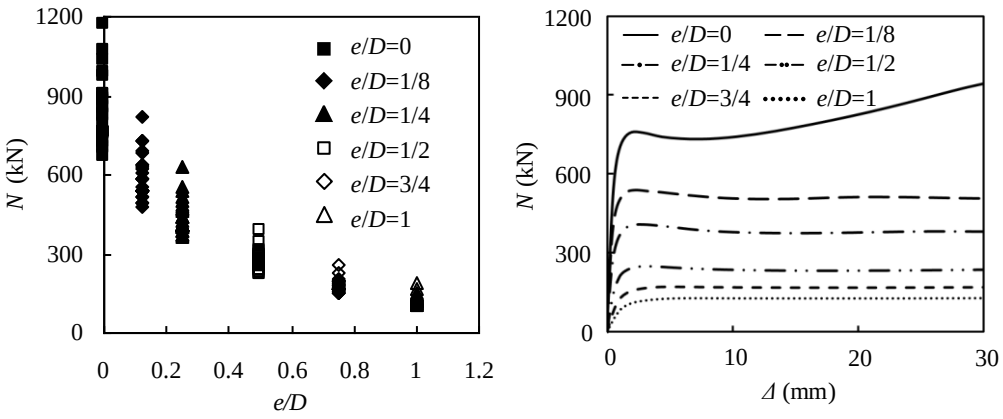

(a) (b)

Fig. 13. Effect of *e*/*D*: (a) *N*-*e*/*D* relationships; (b) *N*-*Δ* relationships

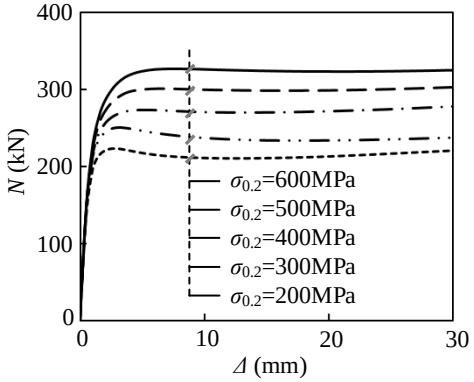

Fig. 14. Effect of $\sigma_{0.2}$.

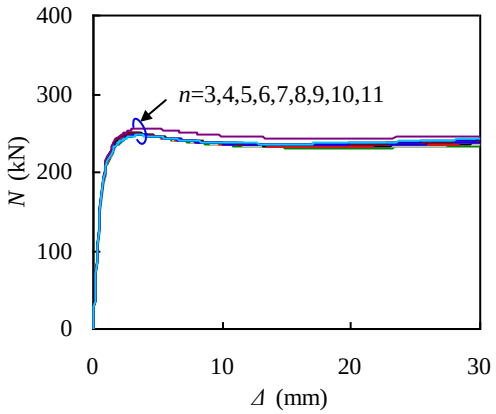

Fig. 15. Effect of *n*.

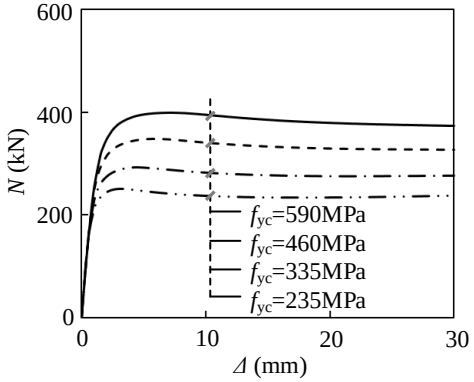

Fig. 16. Effect of f_y.

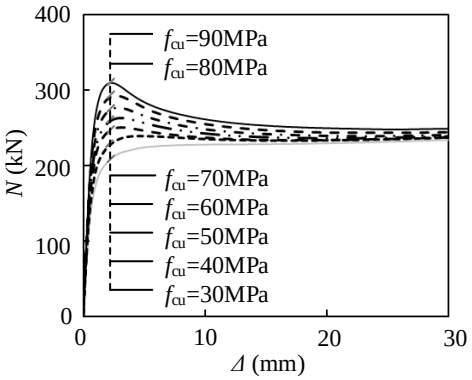

Fig. 17. Effect of f_{cu}.

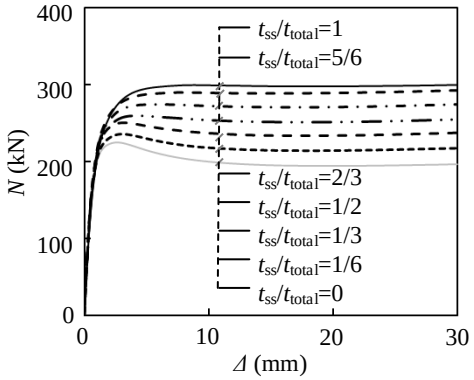

Fig. 18. Effect of t_{ss}/t_{total}.

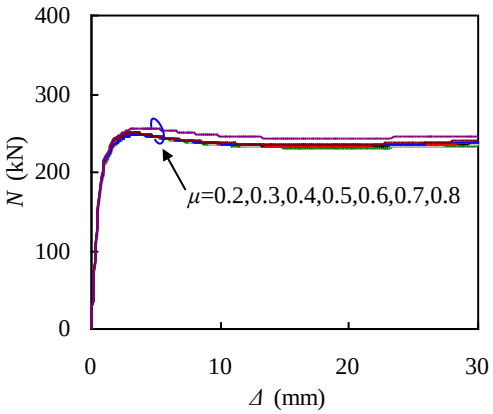

Fig. 19. Effect of μ.

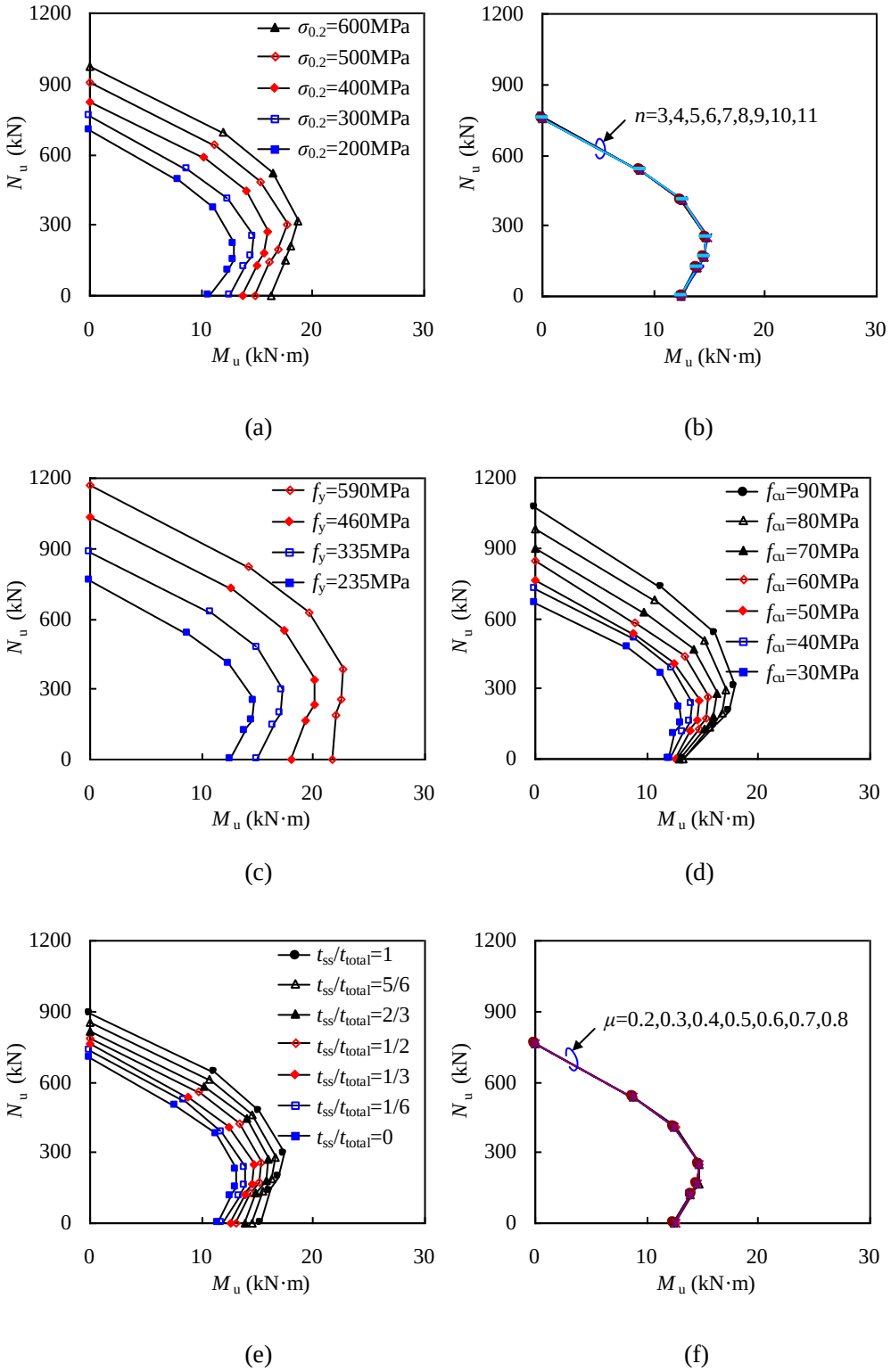

Fig. 20. Influences of different parameters on N_u-M_u relationships: (a) $\sigma_{0.2}$; (b) n; (c) f_y; (d) f_{cu}; (e) t_{ss}/t_{total}; (f) μ.

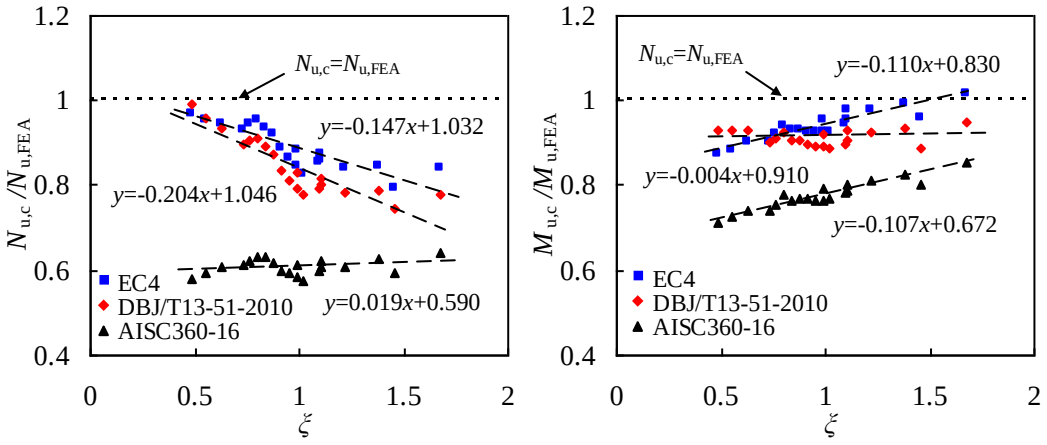

(a) (b)

Fig. 21. Comparison of eccentric strengths between predicted values ($N_{u,c}$) and FEA results ($N_{u,FEA}$): (a) e/D=0.25; (b) e/D=1.

Click here to access/download;Table;Revised Tables.doc

Tables

Table 1 Comparison of ultimate capacities between experimental ($N_{u,e}$) and FEA results ($N_{u,FEA}$)

Specimen label	f_{cu} /MPa	e_n/D	$N_{u,e}$ /kN	$N_{u,FEA}$ /kN	$N_{u,FEA}/N_{u,e}$	Average $N_{u,FEA}/N_{u,e}$	Standard deviation
BT-1	-	0	272.5	273.3	1.003		
BT-e0.26-1	-	0.26	152.5	160.4	1.052		
BT-e0.26-2	-	0.26	155.6	160.4	1.031		
BT-e0.53-1	-	0.53	125.3	118.7	0.947		
BT-e0.53-2		0.53	110.4	118.7	1.075		
BT-e0.79-1	-	0.79	84.6	89.6	1.059		
BT-e0.79-2	-	0.79	87.1	89.6	1.029		
CFBT-1	50	0	774.6	741.4	0.974	1.037	0.064
CFBT-2	50	0	713.3	741.4	1.057		
CFBT-e0.26-1	50	0.26	378.6	448.1	1.200		
CFBT-e0.26-2	50	0.26	397.3	448.1	1.143		
CFBT-e0.53-1	50	0.53	257.5	252.1	0.983		
CFBT- e0.53-2	50	0.53	238.5	252.1	1.061		
CFBT-e0.79-1	50	0.79	188.8	182.2	0.977		
CFBT-e0.79-2	50	0.79	173.4	182.2	1.063		

Table 2a Comparison of ultimate axial loads between experimental and code-calculated results

Specimen label	$N_{u,e}$ /kN	$N_{u,AISC}$ /kN	$N_{u,EC4}$ /kN	$N_{u,DBJ}$ /kN	$N_{u,AISC}/N_{u,e}$	$N_{u,EC4}/N_{u,e}$	$N_{u,DBJ}/N_{u,e}$	Average $N_{u,AISC}/N_{u,e}$	Standard deviation	Average $N_{u,EC4}/N_{u,e}$	Standard deviation	Average $N_{u,DBJ}/N_{u,e}$	Standard deviation
CFBT-1	774.6	530.5	731.8	660.0	0.685	0.945	0.852	0.517	0.243	1.072	0.115	0.953	0.091
CFBT-2	713.3	533.9	734.2	662.3	0.749	1.029	0.929						
CFBT-e0.26-1	378.6	152.8	460.6	405.4	0.404	1.217	1.071						
CFBT-e0.26-2	397.3	91.1	435.5	381.9	0.229	1.096	0.961						

Table 2b Comparison of ultimate moments between experimental and code-calculated results

Specimen label	$M_{u,e}$ /kN·m	$M_{u,AISC}$ /kN·m	$M_{u,EC4}$ /kN·m	$M_{u,DBJ}$ /kN·m	$M_{u,AISC}/M_{u,e}$	$M_{u,EC4}/M_{u,e}$	$M_{u,DBJ}/M_{u,e}$	Average $M_{u,AISC}/M_{u,e}$	Standard deviation	Average $M_{u,EC4}/M_{u,e}$	Standard deviation	Average $M_{u,DBJ}/M_{u,e}$	Standard deviation
CFBT-e0.53-1	16.87	9.35	14.98	14.40	0.554	0.888	0.853	0.617	0.054	0.915	0.019	0.876	0.015
CFBT- e0.53-2	16.51	9.75	15.21	14.54	0.591	0.921	0.881						
CFBT-e0.79-1	16.57	10.81	15.45	14.69	0.652	0.933	0.886						
CFBT-e0.79-2	16.63	11.14	15.27	14.66	0.670	0.918	0.882						